Solar Phys (2012) 277:205–226
DOI 10.1007/s11207-011-9920-5

Vorticity of Subsurface Flows of Emerging and Decaying Active Regions

R. Komm · R. Howe · F. Hill

Received: 15 September 2011 / Accepted: 30 November 2011 / Published online: 22 December 2011

Abstract We study the temporal variation of the vorticity of subsurface flows of 828 active regions and 977 quiet regions. The vorticity of these flows is derived from measured subsurface velocities. The horizontal flows are determined by analyzing high-resolution *Global Oscillation Network Group* Doppler data with ring-diagram analysis covering a range of depths from the surface to about 16 Mm. The vertical velocity component is derived from the divergence of the measured horizontal flows using mass conservation. We determine the change in unsigned magnetic flux density during the disk passage of each active region using *Michelson Doppler Imager* (MDI) magnetograms binned to the ring-diagram grid with centers spaced by 7.5° ranging ±52.5° in latitude and central meridian distance with an effective diameter of 15° after apodization. We then sort the data by their flux change from decaying to emerging flux and divide the data into five subsets of equal size. We find that the vorticity of subsurface flows increases during flux emergence and decreases when active regions decay. For flux emergence, the absolute values of the zonal and meridional vorticity components show the most coherent variation with activity, while for flux decrease the strongest signature is in the absolute values of the meridional and vertical vorticity components. The temporal variation of the enstrophy (residual vorticity squared) is thus a good indicator for either flux increase or decrease. There are some indications that the increase in vorticity during flux emergence happens about a day later at depths below about 8 Mm compared to layers shallower than about 4 Mm. This timing difference might imply that the vorticity signal analyzed here is caused by the interaction between magnetic flux and turbulent flows near the solar surface. There are also hints that the vorticity decrease during flux decay begins about a day earlier at layers deeper than about 8 Mm compared to shallower ones. However, the timing difference between the change at different depths is comparable to the time step of the analysis.

R. Komm (✉) · F. Hill
National Solar Observatory, Tucson, AZ 85719, USA
e-mail: komm@nso.edu

R. Howe
University of Birmingham, Birmingham, UK

Keywords Active regions, velocity field · Helioseismology, observations · Velocity fields, interior

1. Introduction

Previous studies have shown that solar subsurface flows associated with active regions are highly twisted. At locations of high magnetic flux, subsurface flows show large values of vorticity (curl of the velocity vector). For example, locations of high magnetic flux show excess cyclonic vertical vorticity (Duvall and Gizon, 2000; Gizon and Duvall, 2003; Braun, Birch, and Lindsey, 2004; Komm *et al.*, 2004a; Zhao and Kosovichev, 2004), which is clockwise in the northern hemisphere and is most likely due to the Coriolis force acting on the flows. The twist of subsurface flows, as measured by vorticity, also plays a role in the dynamic behavior of active regions. For example, the maximum vorticity of subsurface flows is related to the total flare intensity of active regions (Mason *et al.*, 2006), and the kinetic helicity density, the scalar product of vorticity and velocity, provides timing information about flare activity (Reinard *et al.*, 2010). The temporal evolution of the twist of subsurface flows is less well studied, and these studies have been limited to a handful of active regions (Zhao and Kosovichev, 2003; Komm *et al.*, 2004b). Here, we study the temporal variation of the vorticity of subsurface flows and their relation to emerging and decaying magnetic flux using a large sample of active and quiet regions.

In a previous study (Komm, Howe, and Hill, 2011), we focused on the temporal variation of the velocity vector and found that emerging flux rotates faster than the ambient fluid and pushes it up, as indicated by enhanced vertical velocity and faster-than-average zonal flow. Emerging flux in existing active regions shows a similar scenario, where the upflows at depths greater than about 10 Mm are enhanced and the already-established downflows at shallower depths are weakened. This agrees with numerical simulations (Fan, 2004; Schüssler and Rempel, 2005), where upflows or a diverging pattern of horizontal flows will indicate the beginning of flux emergence, and surface cooling due to adiabatic expansion leads to downflows along the emerged loops. When active regions decay, the corresponding flow pattern disappears as well; the zonal flow slows to values comparable to that of quiet regions and the upflows become weaker at deeper layers. With ring-diagram analysis applied to high-resolution *Global Oscillation Network Group* (GONG++) data, we have established this behavior on spatial scales comparable to the size of active regions. On smaller spatial scales comparable to the size of sunspots, the subsurface flows are more complicated (Gizon *et al.*, 2009; Hindman, Haber, and Toomre, 2009).

The twist of subsurface flows might serve as a proxy for the twist of magnetic flux tubes below the solar surface, because either the flows have to respond to the presence of magnetic fields or the fields are being pushed and twisted by subsurface turbulent flows. The nonzero kinetic helicity of subsurface flows plays a crucial role in a possible mechanism for the second scenario (Longcope, Fisher, and Pevtsov, 1998; Fisher *et al.*, 1999). Strong active regions have associated subsurface flows with large values of zonal and meridional vorticity. Both vorticity components show a distinct dipolar pattern and three distinct ranges in depth (Mason *et al.*, 2006). The near-surface layers (with depths less than about 2 Mm) and the deeper layers (with depths greater than about 7 Mm) show vorticity values of the same sign, while the sign is opposite in the intermediate layers. This has led us to interpret the flow and vorticity pattern associated with active regions as stacked vortex rings with opposite sense of horizontal vorticity (Komm *et al.*, 2011a). The vertical vorticity component is rather small by comparison due to the large size of the analysis areas in the horizontal direction.

To determine the vorticity of subsurface flows, we measure the horizontal velocity components analyzing GONG++ data with the ring-diagram technique and then derive the vertical velocity component from the divergence of the horizontal flows (Komm *et al.*, 2004a). As in a previous study (Komm, Howe, and Hill, 2011), we use a data set of 828 active regions and study the temporal variation of magnetic flux and associated subsurface flows of these regions. We determine the change in unsigned magnetic flux density during the disk passage of each active region using magnetograms obtained from the *Michelson Doppler Imager* (MDI) instrument and sort the data by their average change in activity from emerging to decaying flux. We then divide the sorted data set into five subsets of equal size. Each of these subsets is large enough to generate statistically significant results (Birch, Braun, and Fan, 2010). As a control set, we compare the results with the temporal variation of subsurface flows of 977 quiet regions. Here, we focus on the variation of the vorticity components of these active and quiet regions during their disk passage and study the variation of the vorticity vector in relation to emerging and decaying magnetic activity.

2. Data and Analysis

2.1. Subsurface Vorticity Measurements

We use the same analysis technique outlined in Komm, Howe, and Hill (2009, 2011) and limit the description to the essential parts. We analyze observations obtained during 81 Carrington rotations (1979 – 2059: 27 July 2001 – 14 August 2007) for which we have high-resolution full-disk Doppler data from the GONG network (http://gong.nso.edu/data). We determine the horizontal components of solar subsurface flows with a ring-diagram analysis using the dense-pack technique (Haber *et al.*, 2002) adapted to GONG++ data (Corbard *et al.*, 2003). The full-disk Doppler images are divided into 189 overlapping regions with centers spaced by 7.5° ranging ±52.5° in latitude and central meridian distance (CMD) with an effective diameter of 15° after apodization. The analysis is carried out on overlapping "days" of 1664-minute time periods, and the shift between two days corresponds to exactly 15° of Carrington longitude. For each dense-pack day, we derive daily maps of horizontal velocities at 16 depths from 0.6 to 16 Mm. To focus on the variation of the flows near active regions, we have to remove the average rotation rate and meridional flow. For this purpose, we calculate low-order polynomial fits in latitude of the large-scale flows averaged over each synoptic map. We then calculate daily maps of residual horizontal velocities subtracting these low-order polynomial fits. The residual vertical velocity is then estimated from the divergence of the residual horizontal flows assuming mass conservation (Komm *et al.*, 2004a).

The vorticity vector is defined as the curl of the velocity vector ($\boldsymbol{v}$):

$$\boldsymbol{\omega} = \nabla \times \boldsymbol{v} \tag{1}$$

and is calculated from the residual velocities. The vorticity is a vector quantity that corresponds to changing orientation in space of fluid particles and is thus a quantity associated with mixing and turbulence (Lesieur, 1987, for example). We calculate the vorticity components in spherical coordinates:

$$\omega_r = \frac{1}{r\cos\theta}\left(\frac{\partial}{\partial\theta}[\cos\theta\, v_\phi] - \frac{\partial v_\theta}{\partial\phi}\right) \tag{2}$$

$$\omega_\phi = \frac{1}{r}\frac{\partial}{\partial r}[r v_\theta] - \frac{1}{r}\frac{\partial v_r}{\partial \theta}, \tag{3}$$

$$\omega_\theta = \frac{1}{r\cos\theta}\frac{\partial v_r}{\partial \phi} - \frac{1}{r}\frac{\partial}{\partial r}[r v_\phi], \tag{4}$$

where r, ϕ, and θ are radius, longitude, and latitude. The three components represent the vorticity in the radial, zonal, and meridional directions. Given the difference between horizontal and radial resolution, the two horizontal vorticity components are dominated by the radial gradients of the horizontal velocities, and the radial vorticity component is smaller than the other two. (We refer to depth and not radius in Section 3 and use the term vertical component instead of radial.) We also calculate the enstrophy, which is defined as the residual vorticity squared:

$$\omega^2 = \sum_{k=r,\phi,\theta} \omega_k^2. \tag{5}$$

While enstrophy is a quantity mainly used in the discussion of two-dimensional turbulent flows (Lesieur, 1987), we use it simply as a measure of the strength of vorticity.

2.2. Active and Quiet Regions

We use MDI magnetograms with 96 minutes cadence as a measure of solar activity (http://soi.stanford.edu/magnetic/index5.html). We convert the magnetogram data to absolute values and bin them into circular areas with 15° diameter centered on the same grid as the dense-pack mosaic and average them in time to match the length of a dense-pack day (Howe *et al.*, 2004, 2011). In this way, we estimate a value of the unsigned magnetic flux density (in gauss) called a magnetic activity index (MAI) for each active and quiet region and its temporal variation.

As in Komm, Howe, and Hill (2011), we use a data set of 828 active regions where the complete disk passage is available in flux and flow measurements. The regions have been identified using the NOAA active region numbers. The total number of NOAA active regions during this epoch is about 1400 (9543 – 10 968), but not all of them could be identified or isolated in synoptic maps. As a control set, we select 977 quiet regions with the lowest average MAI values in the same latitude range as the active regions. The disk passage of a particular dense-pack patch takes six or seven dense-pack days ranging from – 37.5° to 37.5° CMD or from – 45° to 45° CMD, respectively.

We sort the data set by the average change in magnetic flux density during the disk passage of each active or quiet region. For the time series of each region, we determine the maximum and minimum MAI values and average over the values before the first extremum and the values after the last one. The difference between the two values is then a measure of the average decrease or increase in magnetic activity during the disk passage of each region. With this definition, we have 330 active regions with increasing activity and 498 active regions with decreasing activity. We divide the data into five subsets of equal size (Table 1). We focus on the subset with the largest increase in activity (subset 1), called the emerging-flux subset, and the subset with the largest decrease (subset 5), called the decaying-flux subset. The other three subsets have on average lower activity levels and smaller changes during their disk passage than either the decaying or the increasing subset. The flux density and flux-density difference values of the quiet regions are about two orders of magnitude smaller than the corresponding values of active regions (Table 2).

Figure 1 shows the distribution of active regions with time and latitude. The active regions are located within ± 30° latitude during cycle maximum and within ± 15° latitude during

Table 1 A set of 828 active regions sorted into five subsets by the average difference (increase or decrease) in magnetic flux density (MAI) during the disk passage of each active region (top). The emerging-flux subset [subset 1] is further divided into an emerging-region subset [1a] and an emerging-flux-in-existing-region subset [1b] (bottom).

Subset	N	MAI (G)			Difference (G)		
		Average	Min.	Max.	Average	Min.	Max.
	828	32.5 ± 27.0	0.6	203.1	-1.5 ± 22.0	−81.3	159.2
1	166	35.6 ± 28.2	5.3	203.1	29.3 ± 22.1	11.5	159.2
2	165	21.0 ± 22.1	0.6	119.2	5.1 ± 3.2	−1.0	11.4
3	166	18.1 ± 12.6	2.7	71.3	-3.8 ± 1.7	−6.8	−1.0
4	165	29.6 ± 16.8	7.0	123.0	-10.2 ± 2.1	−14.3	−6.8
5	166	58.2 ± 30.2	14.1	185.4	-27.7 ± 12.4	−81.3	−14.4
1: emerging flux; 3: low activity; 5: decaying flux							
1a	83	18.2 ± 11.2	5.3	74.6	28.7 ± 22.4	11.7	159.2
1b	83	53.0 ± 29.4	20.1	203.1	29.9 ± 21.9	11.5	104.1
1a: emerging regions; 1b: emerging flux in existing regions							

Table 2 A set of 977 quiet regions sorted into five subsets by the average difference (increase or decrease) in magnetic flux density (MAI) during the disk passage of each quiet region (compare with Table 1).

Subset	N	MAI (G)			Difference (G)		
		Average	Min.	Max.	Average	Min.	Max.
	977	0.46 ± 0.11	0.19	0.79	-0.01 ± 0.29	−0.78	0.59
1	195	0.46 ± 0.09	0.23	0.68	0.34 ± 0.08	0.25	0.59
2	196	0.41 ± 0.10	0.20	0.74	0.19 ± 0.03	0.13	0.25
3	195	0.43 ± 0.12	0.19	0.77	0.03 ± 0.07	−0.09	0.13
4	196	0.47 ± 0.10	0.22	0.78	-0.17 ± 0.05	−0.27	−0.09
5	195	0.54 ± 0.11	0.33	0.79	-0.44 ± 0.13	−0.78	−0.27

cycle minimum. Nevertheless, most active regions (607 of 828) are located at 7.5° to 15° latitude (summed over both hemispheres). The symbol size of the emerging- and decaying-flux subsets indicates the number of active regions per Carrington rotation, which gives some idea of the most populated latitudes and epochs. Most active regions of the two subsets are located at 7.5° to 15° latitude (121 emerging- and 129 decaying-flux regions of 166 regions). Since the regions of the decaying-flux and emerging-flux subsets cover the same epoch and latitude range, we expect that the resulting differences between the two subsets are not due to the distribution of the regions.

In Komm, Howe, and Hill (2011), we were able to distinguish between newly emerging active regions and new flux emerging in existing active regions. We have attempted this distinction with the vorticity data as well. But, we have found that the vorticity data are noisier than the velocity data, as a result of taking the derivative of the velocity data. As a consequence, the further subdivided vorticity subsets for emerging and decaying activity lead to less coherent results and are not discussed in this study except briefly in the last section.

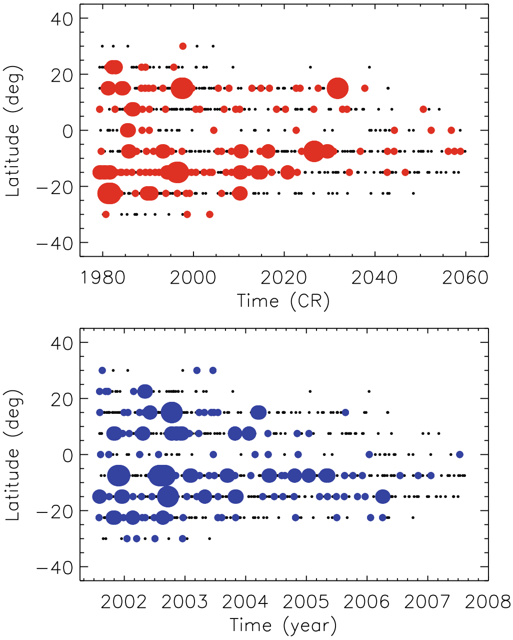

Figure 1 The locations of active regions as a function of time and latitude for all regions of the decaying-flux (top) and emerging-flux subsets (bottom). The small filled circles indicate the locations of all 828 active regions used in this study. The sizes of the symbols of the two subsets indicate the number of regions per Carrington rotation. The time coordinate is given in Carrington rotations (top) and calendar years (bottom).

In this study, we focus on the emerging- and the decaying-flux subsets. For each region, we perform a superposed-epoch analysis using a 10% MAI increase or decrease as the center date. This allows us to align the time series of all regions within a given subset. A consequence of this procedure is that the number of regions contributing to the average time series changes from day to day and is skewed toward the days after the center date. To avoid spurious results, we require that at least one third of all regions of a particular subset contribute to a given day of the average time series. However, it is important to keep in mind that the first and the last day of each time-shifted series have less weight than the other days.

2.3. Variation with CMD and Depth

As in our previous study, we must remove any spatial trend across the disk (in CMD) from the vorticity and activity measurements that could be mistaken for a temporal variation. We determine large-scale trends fitting each quantity with a function consisting of terms in cosine of CMD and a term linear in CMD (Komm, Howe, and Hill, 2009). Figure 2 shows the average vorticity components as a function of CMD at three depths averaged over all active regions (left). The zonal and the vertical vorticity components show a simple center-to-limb variation, while the meridional component shows an east-west asymmetry, which is most likely a consequence of the east-west asymmetry of the zonal velocity component (Komm, Howe, and Hill, 2011). We detrend the vorticity data at a given depth by subtracting the corresponding fit as a function of CMD and then add the disk-averaged vorticity value at this depth.

The disk-averaged value at a given depth is defined as the vorticity averaged over all disk positions weighted by $\cos^4(\mathrm{CMD})$ as in the case of NSO/Kitt Peak synoptic magnetic flux maps. The disk-averaged values are shown on the right-hand side of Figure 2 as a function of depth. The average zonal and meridional vorticity components show a three-layer structure with sign changes near about 2 and 6 Mm, as expected from previous studies of strong active

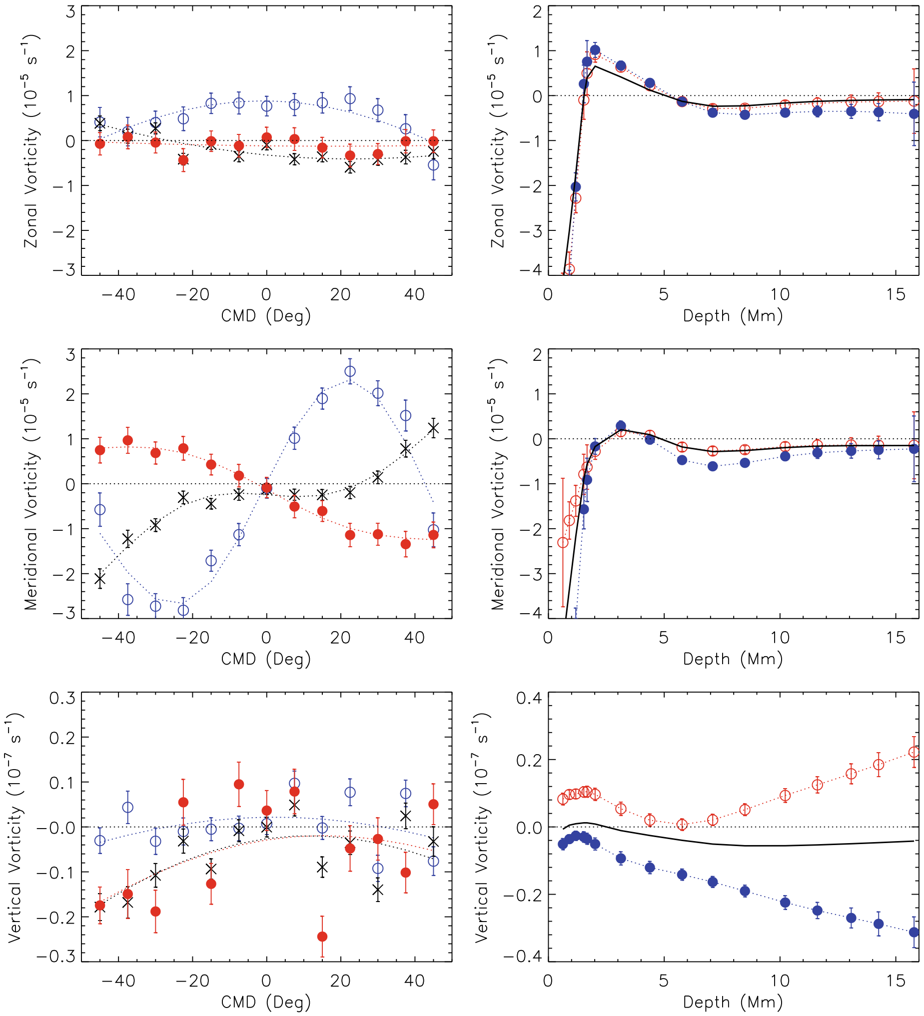

Figure 2 The average zonal (top), meridional (middle), and vertical vorticity (bottom) of active regions. Left: as a function of central meridian distance (CMD) at three depths (open circles: 2 Mm; crosses: 7 Mm; filled circles: 13 Mm). Dotted lines indicate polynomial fits. Right: as a function of depth (solid line) compared to the average values of two subsets (open circles: flux decrease; filled circles: flux increase).

regions (Mason *et al.*, 2006). The emerging- and decreasing-flux subsets show a similar variation with depth. This is in contrast to the vertical vorticity component, where the two subsets have average values of the same sign throughout the depth range but with opposite sign from each other. However, the vertical vorticity component of active regions shows a slight asymmetry between the northern and southern hemisphere in synoptic maps, and the other two components show dipolar patterns of opposite sign in either the latitudinal or longitudinal direction. These patterns can influence the average value since we use a single grid point as the location of each region and do not attempt to sort their vorticity values by the sign.

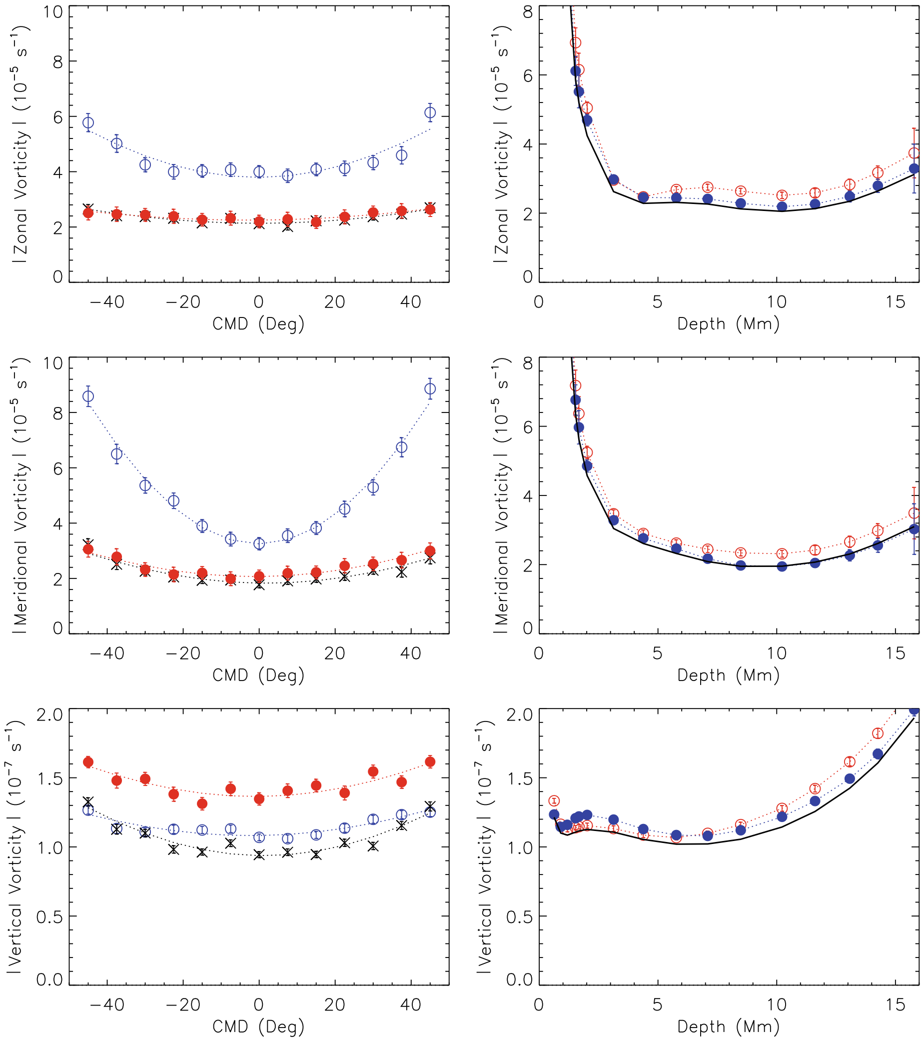

Figure 3 The average unsigned zonal (top), meridional (middle), and vertical vorticity (bottom) of active regions. Left: as a function of CMD at three depths (open circles: 2 Mm; crosses: 7 Mm; filled circles: 13 Mm). Dotted lines indicate polynomial fits. Right: as a function of depth (solid line) compared to the average values of two subsets (open circles: flux decrease; filled circles: flux increase). (Compare with Figure 2.)

We expect that the magnitude, and not the sign, of vorticity matters when comparing vorticity with the evolution of magnetic activity. Figure 3 shows the same information as Figure 2 using the absolute values of each vorticity component. In this case, all three components show simple center-to-limb variations. Compared to Figure 2, the CMD variations show less fluctuation and are better represented by the polynomial fits, which is especially true for the vertical vorticity component. The decaying active regions have slightly stronger vorticity values than the emerging regions. The average values over all regions are slightly smaller than averages of the two subsets, which indicates that the other three subsets have less vorticity than either the decaying- or the increasing-flux subset. This coincides with the

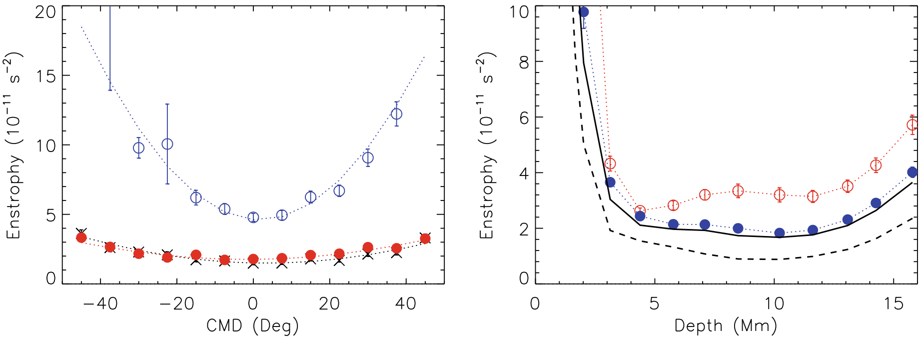

Figure 4 The average enstrophy of active regions. Left: as a function of CMD at three depths (open circles: 2 Mm; crosses: 7 Mm; filled circles: 13 Mm). Dotted lines indicate polynomial fits. Right: as a function of depth (solid line) compared to the average values of two subsets (open circles: flux decrease; filled circles: flux increase). The average values for quiet regions (dashed line) are included for comparison. (Compare with Figure 3.)

fact that the average level of magnetic activity of the emerging-flux subset is smaller than that of the decaying subset but greater than that of the grand average (see Table 1). The absolute values of the subsurface vorticity of quiet regions (not shown) are of course smaller than the corresponding values of active regions but show similar CMD and depth variations. From now on, we use the absolute values of the vorticity to measure the size of vorticity and its temporal variation.

Figure 4 shows the same information as Figure 3 for the enstrophy. Since this quantity is dominated by the zonal and the meridional vorticity component, its depth variation is similar to that of the two horizontal components shown in Figure 3. As in the previous figures, the decaying subset has larger values than the emerging one, and the grand average has lower enstrophy values than either subset. The average enstrophy values derived from quiet regions are smaller at all depths than the grand average values of active regions. Also, the enstrophy of quiet regions shows no difference between the corresponding two subsets of different magnetic activity (not included in Figure 4).

Now, we check to see whether the depth variation of the horizontal vorticity components might be biased by edge effects due to taking derivatives in the radial direction on a nonuniform grid. The qualitative behavior is probably not influenced by such numerical effects, since the systematic dipolar pattern in depth of the horizontal vorticity components is noticeable in all strong active regions and absent from quiet ones. This characteristic vorticity pattern is not only present in GONG data but also in MDI data analyzed with a different inversion technique and depth grid (Haber *et al.*, 2004). As a quantitative test, we have randomized the residual velocities at each depth of two Carrington rotations (1988 and 2074) representing flows during solar maximum and minimum and we have calculated the vorticity of the randomized sets. The individual vorticity components of the randomized data show fluctuations on horizontal scales comparable to the dense-pack grid size, which is on a smaller scale than the variations shown in the original data. As a consequence, synoptic maps of the randomized data of CR 1988 show many locations with high enstrophy values, while the original data show only few locations with high enstrophy values which coincide with locations of strong active regions. Also, the original data show hardly any locations with large enstrophy values in CR 2074 representing cycle minimum, while the corresponding randomized data lead to a distribution similar to that of the randomized data of CR 1988. When plotted as a function of depth, the average enstrophy values of the randomized data

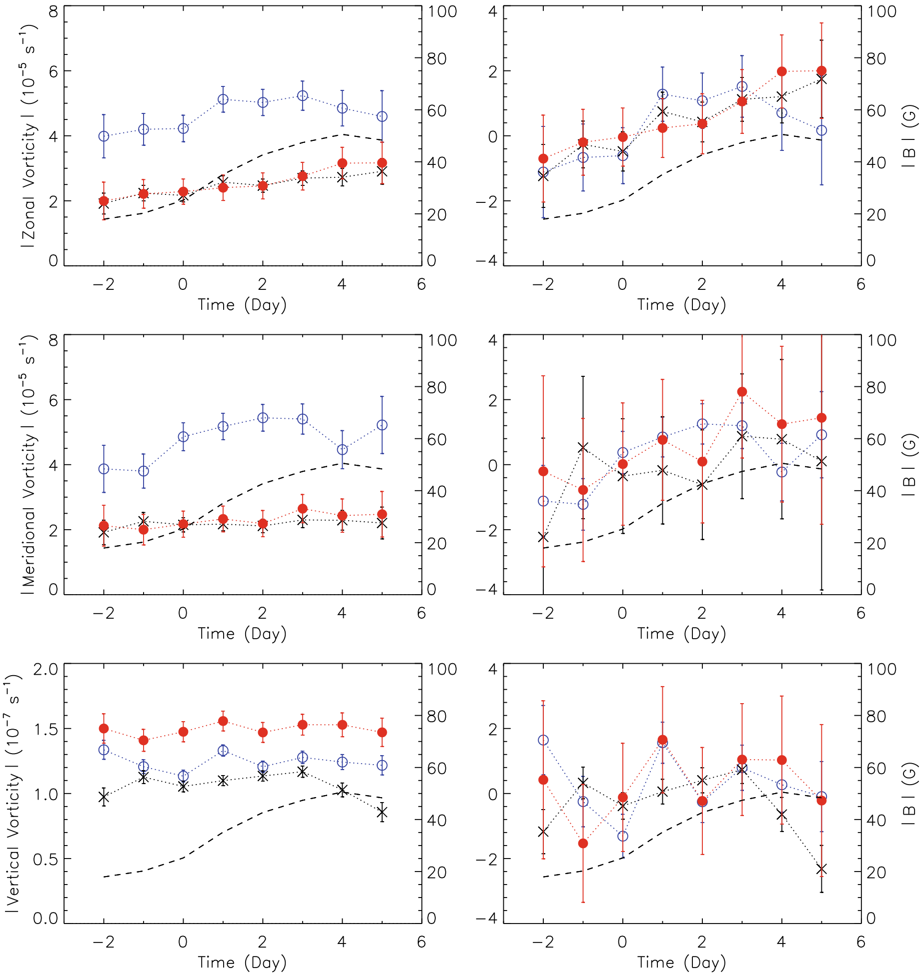

Figure 5 The unsigned zonal (top), meridional (middle), and vertical vorticity (bottom) of active regions at three depths (open circles: 2 Mm; crosses: 7 Mm; filled circles: 13 Mm) averaged over all regions of the emerging-flux subset (left) and the same quantities normalized by the standard deviation of each temporal variation (right). The individual time series are shifted so that day 0 indicates a 10% increase in the magnetic activity index (MAI). The mean of the values of days −1, 0, and +1 has been subtracted from the normalized values. The dashed lines indicate the temporal variation of the MAI.

are about one order of magnitude larger than those of the original data and increase much more strongly at either end of the depth range than the original data. The average variation with depth of the randomized data is the same independent of magnetic activity, while the average enstrophy of the original data is clearly larger during a high-activity epoch than during a low-activity one (Figure 4). In addition, the randomized data show a local maximum near 2 Mm, which is a consequence of using this particular nonuniform grid in depth. This local maximum is absent in the original data. Nevertheless, the test with randomized data shows that the values within 2 Mm of the surface are potentially enlarged due to edge effects and are thus less reliable than the values at other depths. The vertical vorticity component, defined as the curl of the horizontal velocities, is probably not affected by edge effects of

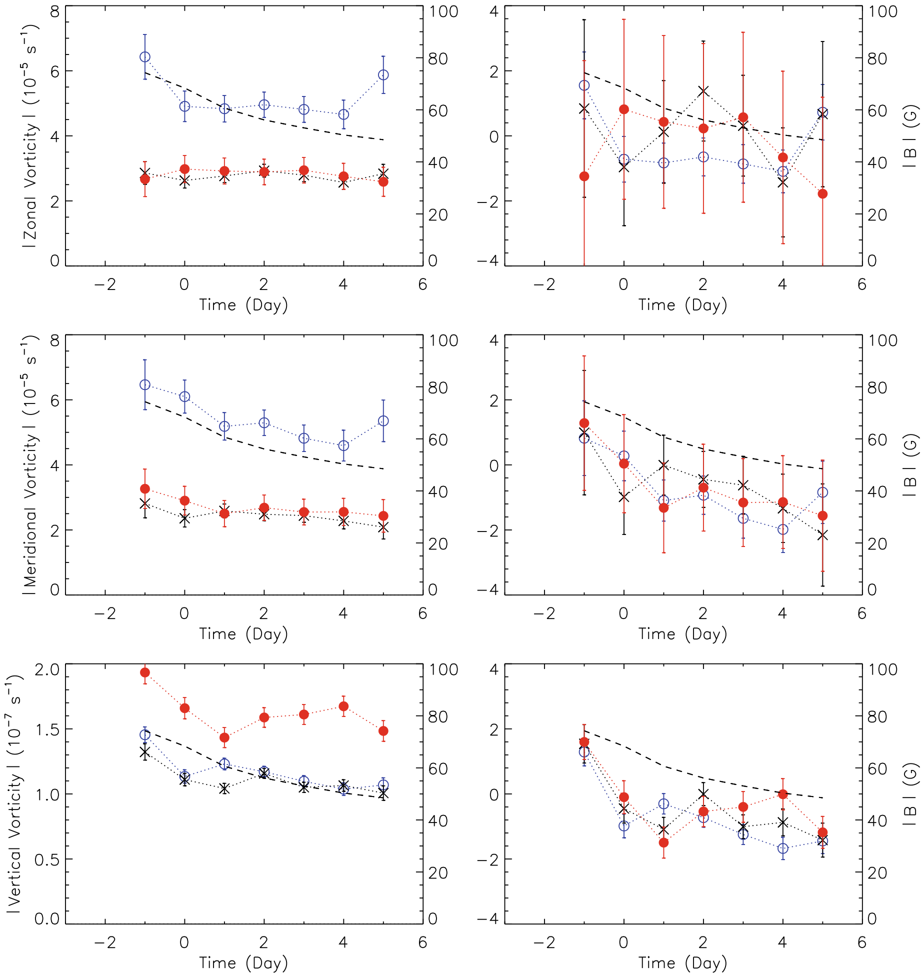

Figure 6 The unsigned zonal (top), meridional (middle), and vertical vorticity (bottom) of active regions at three depths (open circles: 2 Mm; crosses: 7 Mm; filled circles: 13 Mm) averaged over all regions of the decaying-flux subset (left) and the same quantities normalized by the standard deviation of each temporal variation (right). The individual time series are shifted so that day 0 indicates a 10% decrease in MAI. The mean of the values of days −1, 0, and +1 has been subtracted from the normalized values. The dashed lines indicate the temporal variation of the MAI. (Compare with Figure 5.)

the latitude grid, since we are analyzing active and quiet regions within ±30° latitude and not locations at high latitudes.

From this section, we conclude that the average size of vorticity is correlated with the average magnetic field strength of a region. For active regions, the decaying-flux subset is the subset with the largest average MAI and vorticity values compared to any other subset.

3. Results

In this section, we study the temporal variation of the vorticity of subsurface flows averaged over the emerging- and decaying-flux subsets. The spatial trend across the disk (in CMD)

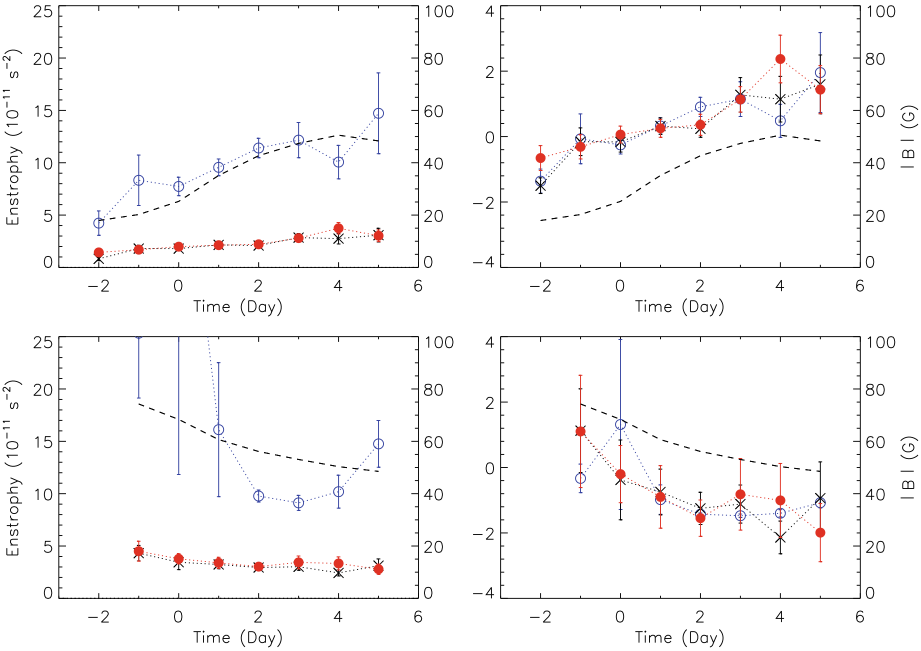

Figure 7 The enstrophy of active regions derived at three depths (open circles: 2 Mm; crosses: 7 Mm; filled circles: 13 Mm) averaged over all regions of the emerging-flux (top left) and the decaying-flux (bottom left) subsets and the same quantities normalized by the standard deviation of each temporal variation (right). The mean of the values of days −1, 0, and +1 has been subtracted from the normalized values. The dashed lines indicate the temporal variation of the MAI. (Compare with Figures 5 and 6.)

has been removed from all active and quiet region data sets used here, as described in Section 2.3. The individual time series are shifted so that day 0 indicates either a 10% increase or decrease in magnetic flux density. For the emerging-flux subset, Figure 5 shows the temporal variation of the absolute values of the three vorticity components at three depths. The zonal and the meridional vorticity components increase with increasing magnetic activity, while the vertical vorticity remains rather flat during the same days. It is difficult to gauge how the rate of the temporal variation varies with depth, since the average vorticity values change with depth. The normalized values shown in the right-hand side of Figure 5 agree within the normalized error bars. The variation with increasing magnetic activity is thus very similar at all three depths. The normalized errors are smaller for the zonal vorticity component than for the other two components, which means that the zonal vorticity component has the most reliable variation of the three components for the emerging-flux subset.

Figure 6 shows the same information as Figure 5 for the decaying-flux subset. In this case, the meridional and the vertical vorticity components decrease with decreasing magnetic activity, while the zonal component remains flat by comparison. The rate of vorticity decrease is similar at all three depths as indicated by the normalized values, which agree within the normalized error bars. The vertical vorticity component shows the smallest normalized error bars compared with the other two components; its temporal variation is large compared to the normalized error. For the decaying-flux subset, the vertical vorticity component has the most reliable variation of the three components.

Figure 7 shows the same information as Figures 5 and 6 for enstrophy, which serves as a measure of the size of vorticity. The temporal variation of enstrophy matches the increase

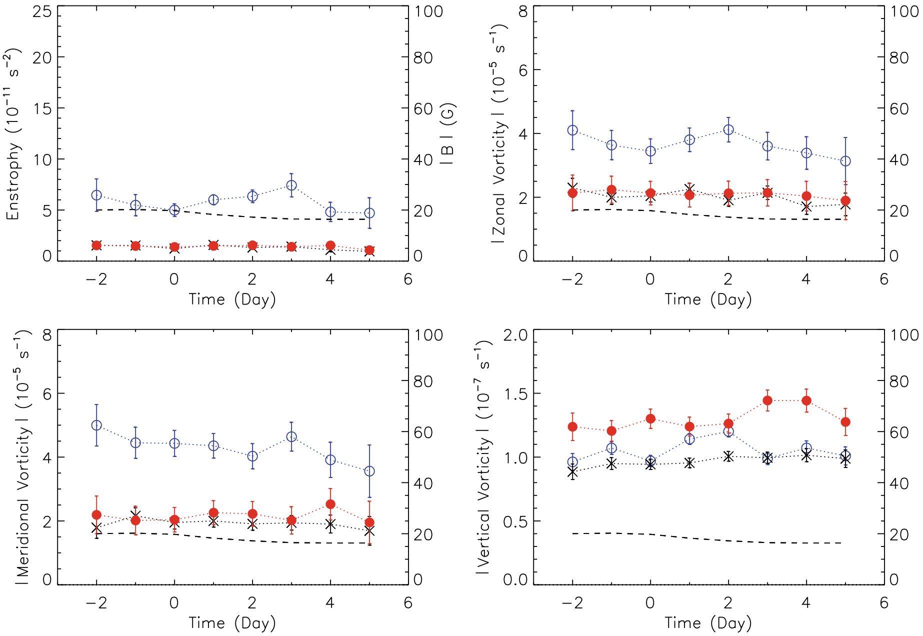

Figure 8 The enstrophy (top left), the unsigned zonal (top right), the unsigned meridional (bottom left), and the unsigned vertical vorticity (bottom right) of active regions at three depths (open circles: 2 Mm; crosses: 7 Mm; filled circles: 13 Mm) averaged over all regions with the lowest magnetic activity. The dashed lines indicate the temporal variation of the MAI. (Compare with Figures 5 through 7.)

or decrease in magnetic activity, as expected from the variation of the individual vorticity components. The variation of the normalized enstrophy is less noisy than that of the individual components for the emerging- and decaying-flux subsets. The normalized enstrophy errors are smaller than those of the individual vorticity components for the emerging-flux subset, while the normalized enstrophy errors are slightly larger than those of the vertical vorticity component for the decaying-flux subset. We thus expect that the enstrophy values are a good indicator of the temporal variation of vorticity.

As a control experiment, we analyze two sets of subsurface flows at locations with low levels of magnetic activity. First, we show in Figure 8 the enstrophy and the three vorticity components for active regions averaged over the low-activity subset (subset 3 in Table 1). The values are small compared to the corresponding values of the emerging- and decaying-flux subsets and are rather constant with time at all three depths for all four parameters. Second, we show in Figure 9 the temporal variation of the enstrophy and the zonal and vertical vorticity components for quiet regions divided into increasing- and decreasing-flux subsets sorted in the same way as active regions (subsets 1 and 5 in Table 2). The values are smaller than the corresponding values for the active regions and show no significant changes with time at all three depths for the studied parameters. The values derived from quiet regions are comparable but slightly smaller than those of the weak active regions shown in Figure 8. These two control experiments show that when the magnetic activity and the activity variations are small, the vorticity values and their temporal variations are small as well.

Now, we focus on the temporal variations of the vorticity at all depths. Figure 10 shows the temporal variation of the three vorticity components for the emerging-flux subset. The

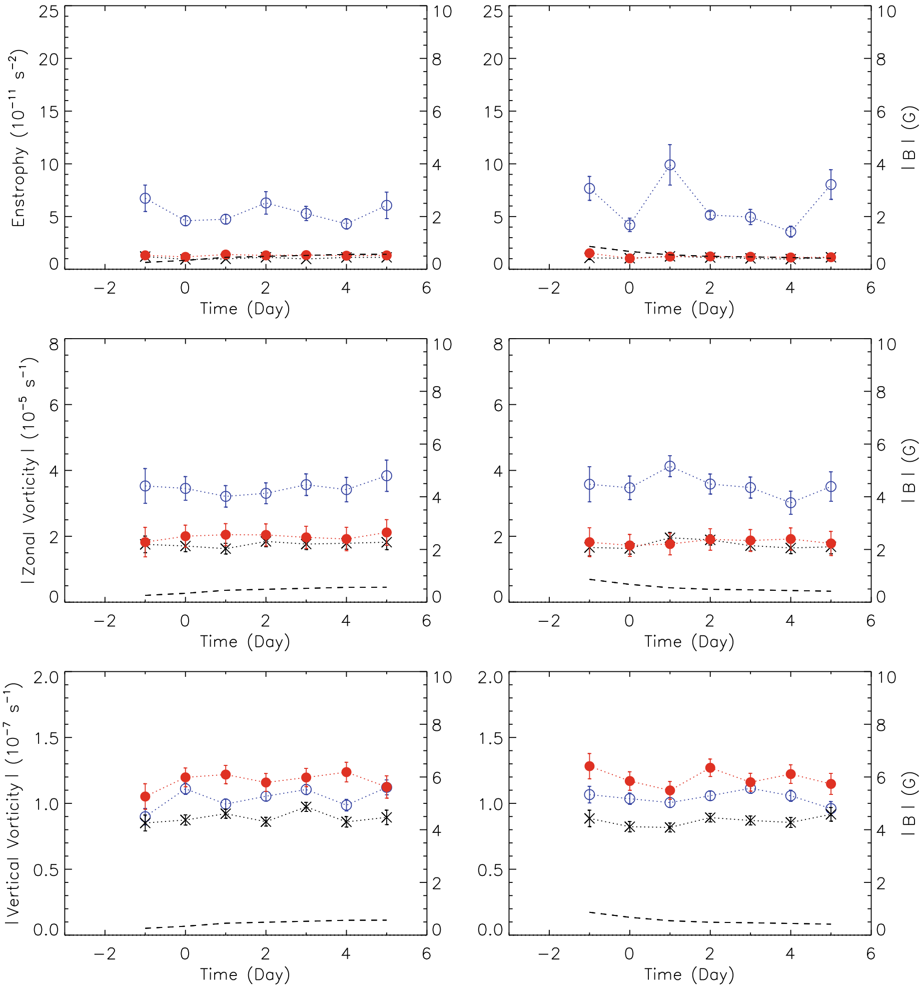

Figure 9 The enstrophy (top), the unsigned zonal (middle), and the unsigned vertical vorticity (bottom) of quiet regions at three depths (open circles: 2 Mm; crosses: 7 Mm; filled circles: 13 Mm) averaged over all regions of the increasing flux (left) and decreasing flux (right) subsets. The individual time series are shifted so that day 0 indicates either a 10% increase (left) or a 10% decrease in MAI (right). The dashed lines indicate the temporal variation of the MAI. (Compare with Figures 5 through 8.)

mean has been subtracted at every depth. The zonal and meridional vorticity components clearly increase with time at all depths, and the zero contour seems to imply that the change occurs first at shallow layers and later at deeper ones. The vertical vorticity shows some variation with time but not a consistent increase with increasing activity. The zonal component shows the most consistent variation with time or magnetic activity.

Figure 11 shows the same information as Figure 10 for enstrophy. The enstrophy values increase with time at all depths, as expected from Figures 7 and 10. The change occurs within about one day at all depths; the zero contour is located near day 1 at the surface and near day 2 at 16 Mm. The 0.8 contour of the normalized values is located between days 1 and 2 at depths shallower than about 4 Mm and between days 2 and 3 at greater depths.

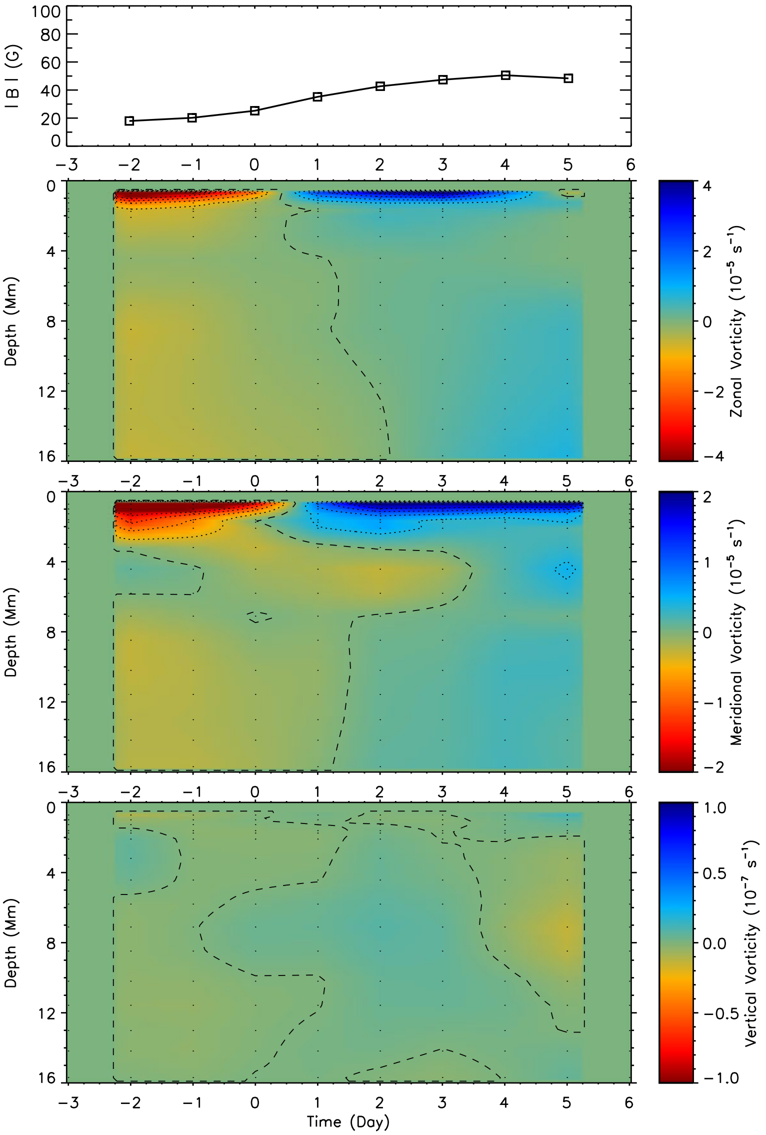

Figure 10 Top: The smoothed variation of the MAI averaged over the emerging-flux subset. Second: The unsigned residual zonal vorticity averaged over the same subset as a function of time and depth. Third: The corresponding unsigned residual meridional vorticity. Bottom: The corresponding unsigned residual vertical vorticity. The mean has been subtracted at every depth. The values have been smoothed (via a three-day moving window averaging) to reduce the noise seen in Figure 5. The dashed lines indicate the zero contour, and the dotted contours are in steps of 20% of maximum or minimum value.

However, the 1.6 contour is located near day 4 at nearly all depths. This seems to imply that the initial increase in vorticity during flux emergence happens first in shallow layers and later in deeper ones, while near the end of the emergence process the vorticity has increased by roughly the same rate at all depths. However, the timing difference between the change at different depths is comparable to the time step of the analysis.

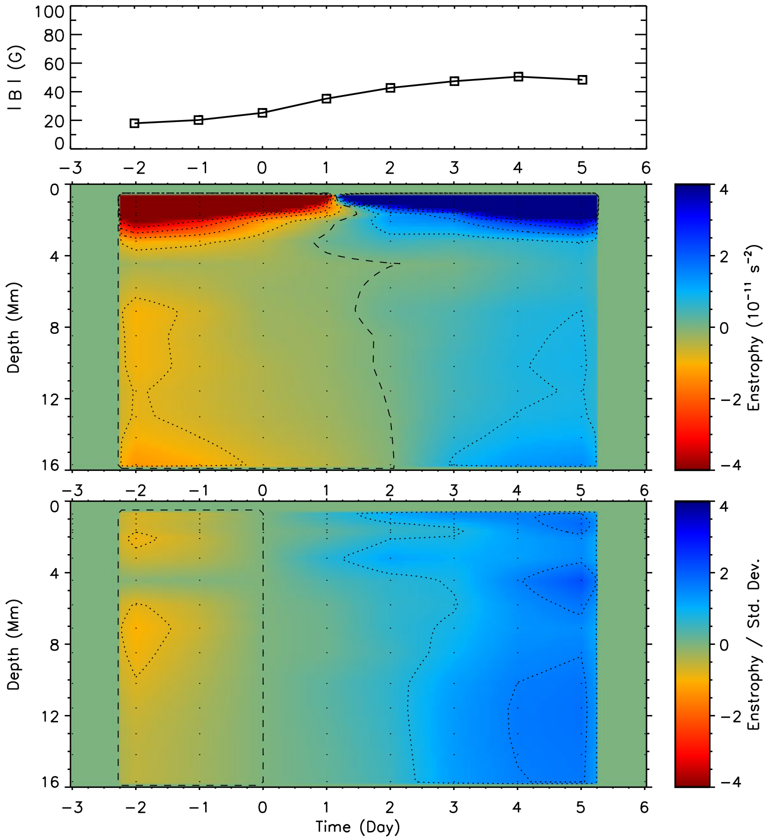

Figure 11 Top: The smoothed variation of the MAI averaged over the emerging-flux subset. Second: The enstrophy averaged over the same subset as a function of time and depth. The mean has been subtracted at every depth. Bottom: The normalized enstrophy. The values have been divided by the standard deviation at each depth, and the mean of the values of days −1, 0, and +1 has been subtracted. The values have been smoothed to reduce the noise seen in Figure 7. The dashed lines indicate the zero contour, and the dotted contours are in steps of 20% of maximum or minimum value.

Figures 12 and 13 show the corresponding temporal variation of vorticity for the decaying-flux subset. As in the two previous figures, the mean values have been subtracted. For the decaying-flux subset, all three vorticity components decrease with decreasing magnetic flux density (Figure 12). In this case, the vertical vorticity component shows the most consistent variation with time or magnetic activity. For the vertical component, the zero contour is near day 0 at 16 Mm and near day 2 at about 4 Mm, which seems to imply that the vorticity decrease starts at deeper layers.

The enstrophy decreases with time at all depths when magnetic activity decreases (Figure 13). The zero contour is located near day 1 at depths greater than about 8 Mm and near day 2 at shallower layers. The normalized enstrophy values show a corresponding earlier decrease in deeper layers than in shallower ones. The enstrophy and the vertical vorticity results thus seem to imply that the decrease in vorticity takes place first at deeper layers and then at shallower ones. The timing difference between the change at different depths is again comparable to the time step of the analysis.

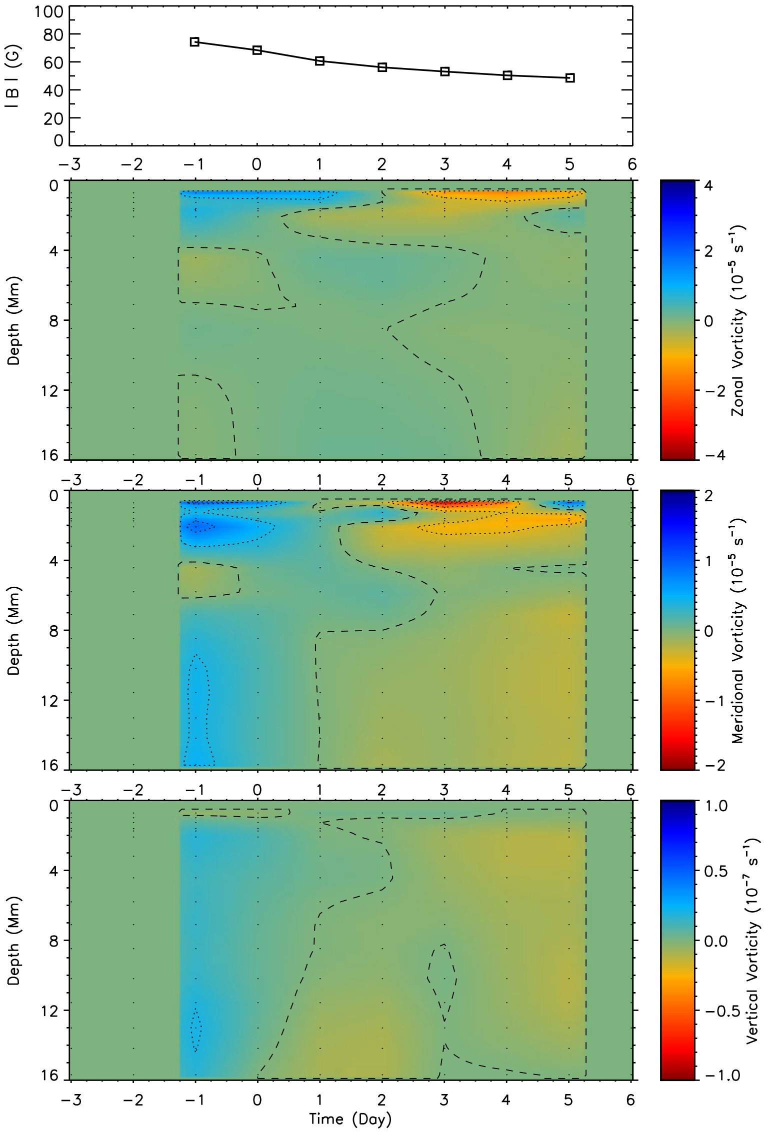

Figure 12 Top: The smoothed variation of the MAI averaged over the decaying-flux subset. Second: The unsigned residual zonal vorticity averaged over the same subset as a function of time and depth. Third: The corresponding unsigned residual meridional vorticity. Bottom: The corresponding unsigned residual vertical vorticity. The mean has been subtracted at every depth. The values have been smoothed to reduce the noise seen in Figure 6. The dashed lines indicate the zero contour, and the dotted contours are in steps of 20% of maximum or minimum value.

At depths between about 4 to 6 Mm, the meridional vorticity shows a relative decrease during days of emergence (days 0 – 3 in Figure 10) and a relative increase during days of decreasing flux density (days 0 – 3 in Figure 12), which is different from the relative increase or decrease with time seen at other depths. As a consequence, the zero contour extends beyond day 2 at the same depth range in the enstrophy variation (Figures 12 and 13). This varia-

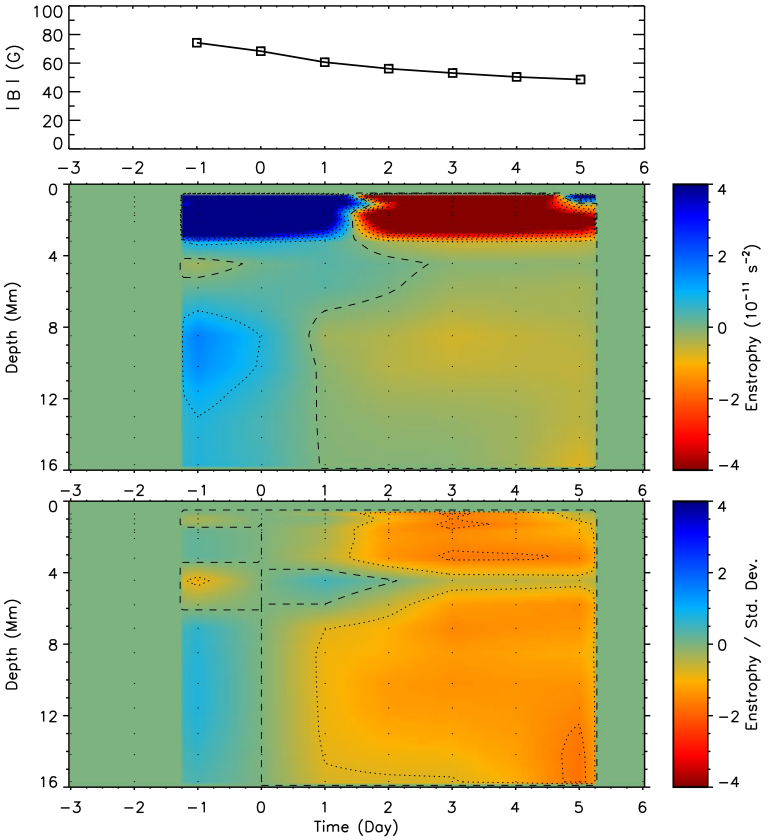

Figure 13 Top: The smoothed variation of the MAI averaged over the decaying-flux subset. Second: The enstrophy averaged over the same subset as a function of time and depth. Bottom: The normalized enstrophy. The values have been divided by the standard deviation at each depth, and the mean of the values of days -1, 0, and $+1$ has been subtracted. The values have been smoothed to reduce the noise seen in Figure 7. The dashed lines indicate the zero contour, and the dotted contours are in steps of 20% of maximum or minimum value.

tion might simply indicate that there are no strong systematic variations in the meridional vorticity component at these depths compared to other depths.

The results for emerging and decaying active regions show that the vorticity of subsurface flows increases or decreases with a corresponding change in magnetic activity. In addition, there are some hints that the change in vorticity occurs at different times at different depths. In both cases, there is a difference of about one day or two between the shallow and deeper layers with regard to the onset of either increase or decrease in vorticity.

4. Summary and Conclusions

The evolution of active regions, especially their emergence, remains one of the major topics of interest in helioseismology (Kosovichev, 2009; Ilonidis, Zhao, and Kosovichev, 2011). We have analyzed a sufficiently large data set to surpass anecdotal evidence and derive statistically significant results. In Komm, Howe, and Hill (2011), we have studied the temporal variation of the velocity vector on dense-pack scales and found that emerging flux rotates faster than the ambient fluid and pushes it up. This is consistent with numerical simulations of emerging flux tubes (Fan, 2004; Schüssler and Rempel, 2005) where upflows or a diverging pattern of horizontal flows indicate the beginning of flux emergence, and surface cooling due to adiabatic expansion leads to downflows along the emerged loops. The characteristic downflow pattern is established within two days after flux emergence (Komm, Howe, and Hill, 2011). Here, we focus on the vorticity of the subsurface flows associated with emerging and decaying magnetic flux.

We follow the analysis outlined in our previous study (Komm, Howe, and Hill, 2009, 2011). We derive the daily variation of all three velocity components for all active and quiet regions from the surface to a depth of about 16 Mm by analyzing GONG++ data and then calculate the vorticity vector from the velocity data. Since the measurements are taken on a dense-pack grid with a spatial scale comparable to the size of active regions, the results reflect the average behavior of active regions summed over many types of magnetic features as well as contributions by the quiet Sun. The impact of strong magnetic fields (sunspots) is thus not as strong in our results as in other helioseismic measurements with high spatial resolution (Gizon and Birch, 2005; Gizon *et al.*, 2009; Moradi *et al.*, 2010).

As control experiments, we have analyzed regions with low magnetic activity. The vorticity values of subsurface flows of quiet regions are small and fluctuate somewhat with time, but they do not show any systematic variation with time. The quiet region values are comparable but slightly smaller than the vorticity values of the subset of weak active regions. The vorticity values of weak active regions are also more or less constant with time. The vorticity values and their temporal variation are small when the magnetic field strength and its variation are small. Since the average magnetic field strength is about an order of magnitude different between quiet regions and weak active regions, this similarity in vorticity values might imply that we have reached a lower limit in our measurements due to the analysis technique. Using high-resolution Dopplergrams obtained with the *Helioseismic and Magnetic Imager* (HMI) instrument onboard the *Solar Dynamics Observatory* (SDO), we plan to repeat the analysis with ring-diagram regions as small as 4° and check whether the vorticity values of quiet regions represent a solar limit or a lower limit of the applied technique.

For the emerging- and decaying-flux subsets, two of the three vorticity components clearly vary with the variation of magnetic activity, while the third one shows a less systematic variation. In the case of the emerging-flux subset, the vertical vorticity is rather constant with time; in the case of the decaying-flux subset, it is the zonal component that is less consistent than the others. To create a smoother temporal variation than possible with the individual vorticity components, we average over all three and calculate the enstrophy. The enstrophy values are dominated by the zonal and meridional vorticity components given the different spatial resolution in the horizontal and vertical directions. We can thus use the enstrophy and the vertical vorticity to represent the information contained in the vorticity measurements.

For the emerging-flux subset, the vorticity amplitude increases with increasing magnetic activity at all depths within 16 Mm of the surface. While the change occurs at all depths within about one day, the zonal vorticity component and the normalized enstrophy values seem to imply that the increase in vorticity happens first in shallow layers and then at deeper ones. For example, the 0.8 contour in the normalized enstrophy plot is located near day 1 at the surface and near day 2 at 16 Mm (Figure 11). However, the time step is also one ring day and thus too long to adequately resolve the difference in onset with depth. When dividing the emerging-flux subset into two subsets of equal size, the timing difference is almost two days in the subset of emerging regions and the timing is nearly the same at all depths in the subset where new flux emerges in existing regions. Taken at face value, this seems to imply that the vorticity increase during the emergence of active regions is a near-surface effect with a downward traveling response. A possible explanation for this behavior is that the flows of the emerging flux have some initial vorticity and create secondary vortex rings by interacting with the flows near the boundary layer between convection zone and atmosphere similar to a head-on collision with a no-slip wall (Shariff and Leonard, 1992). The vorticity pattern observed at deeper layers would then represent secondary vortex rings. If this interpretation is correct, the vorticity measurements might not have much predictive capability when it comes to forecasting the emergence of magnetic activity.

For the decaying-flux subset, the vorticity decreases with decreasing magnetic activity at all depths within 16 Mm of the surface. As in the case of the emerging flux, the vorticity variation is similar at all depths and there is a hint that the change happens at different times at different depths. For example, the 0.8 contour in the normalized enstrophy plot is located near day 2 at depths shallower than about 4 Mm and close to day 1 at depths greater than about 8 Mm (Figure 13). This depth of about 8 Mm dividing shallow and deeper layers is roughly the depth where dynamic disconnection is expected to occur (Schüssler and Rempel, 2005). Since the vorticity decreases first at deeper layers, this might imply that the outflow from the disconnected parent flux tube has stopped (Schüssler and Rempel, 2005) or that the parent flux tube has submerged (van Ballegooijen and Mackay, 2007). However, the timing difference between the change at different depths is again comparable to the time step of the analysis.

The vorticity variation related to activity increase or decrease is not as pronounced at depths between about 4 to 6 Mm in the meridional vorticity component and consequently in the enstrophy. This is the same depth range where the vorticity signal is not a good parameter for distinguishing between flare-productive and nonflaring active regions in contrast to the near-surface or deeper layers (Komm *et al.*, 2011b) and where the meridional and zonal vorticity components change sign (Mason *et al.*, 2006). The vorticity signal might not be as consistent in this depth range as at other depths. But, it also shows that we will need to further improve the signal-to-noise ratio, which might require an even larger sample of active regions.

Here, we clearly show that the vorticity of subsurface flows measured on dense-pack scales reflects the evolution of active regions. However, we have focused strictly on the temporal variation of the strength of vorticity without regard to the question of whether vorticity changes sign during the evolution of active regions. We have done this mainly to avoid spurious results from mixing vorticity values with opposite sign, which can exist within active regions. In the near future, we plan to subdivide the data set by region morphology and to determine the variation of the signed vorticity within each region. For example, we plan to search for a signature of rotating sunspots in the vertical vorticity component of subsurface flows. Sunspots that rotate around their umbral centers have been observed in the solar atmosphere (Brown *et al.*, 2003; Gopasyuk and Kosovichev, 2011), and their associated subsurface motions have been determined in some cases (Jain *et al.*, 2011; Zhao and Kosovichev, 2003). A signature of rotating sunspots might be hidden in the averaged values of the vertical vorticity component shown here, since we average over all regions with emerging flux and not just emerging active regions. Also, we plan to repeat the analysis with better temporal resolution in order to resolve the timing of the vorticity increase during flux emergence.

In addition, we plan to analyze HMI Dopplergrams with smaller ring-diagram patches. With the HMI data, we can study the near-surface layers with better spatial resolution and determine the vorticity values near the surface. All this will allow us to answer the question of whether the measured vorticity is inherent in the flows associated with emerging flux or is generated by the interaction with near-surface turbulent flows.

Acknowledgements This work utilizes data obtained by the Global Oscillation Network Group (GONG) program, managed by the National Solar Observatory, which is operated by the Association of Universities for Research in Astronomy (AURA), Inc. under a cooperative agreement with the National Science Foundation. The data were acquired by instruments operated by the Big Bear Solar Observatory, High Altitude Observatory, Learmonth Solar Observatory, Udaipur Solar Observatory, Instituto de Astrofísica de Canarias, and Cerro Tololo Interamerican Observatory. SOHO is a mission of international cooperation between ESA and NASA. This work was supported by NSF Award No. 1062054 and NASA grant NNG08EI54I to the National Solar Observatory and RK was partialy supported by NASA grant NNX10AQ69G to Alysha Reinard.

References

Birch, A.C., Braun, D.C., Fan, Y.: 2010, *Astrophys. J. Lett.* **723**, L190.
Braun, D.C., Birch, A.C., Lindsey, C.: 2004, In: Danesy, D. (ed.) *Helio- and Asteroseismology: Towards a Golden Future* **SP-559**, ESA, Noordwijk, 337.
Brown, D.S., Nightingale, R.W., Alexander, D., Schrijver, C.J., Metcalf, T.R., Shine, R.A., Title, A.M., Wolfson, C.J.: 2003, *Solar Phys.* **216**, 79.
Corbard, T., Toner, C., Hill, F., Hanna, K.D., Haber, D.A., Hindman, B.W., Bogart, R.S.: 2003, In: Sawaya-Lacoste, H. (ed.) *Local and Global Helioseismology: The Present and Future* **SP-517**, ESA, Noordwijk, 255.
Duvall, T.L. Jr., Gizon, L.: 2000, *Solar Phys.* **192**, 177.
Fan, Y.: 2004, *Living Rev. Solar Phys.* **1**(1). http://solarphysics.livingreviews.org/Articles/lrsp-2004-1.
Fisher, G.H., Longcope, D.W., Linton, M.G., Fan, Y., Pevtsov, A.A.: 1999, In: Núñez, M., Ferriz-Mas, A. (eds.) *Stellar Dynamos: Nonlinearity and Chaotic Flows* **178**, Astron. Soc. Pac., San Francisco, 35.
Gizon, L., Birch, A.C.: 2005, Local Helioseismology. *Living Rev. Solar Phys.* **2**(6). http://solarphysics.livingreviews.org/Articles/lrsp-2005-6.
Gizon, L., Duvall, T.L. Jr.: 2003, In: Sawaya-Lacoste, H. (ed.) *Local and Global Helioseismology: The Present and Future* **SP-517**, ESA, Noordwijk, 43.
Gizon, L., Schunker, H., Baldner, C.S., Basu, S., Birch, A.C., Bogart, R.S., Braun, D.C., Cameron, R., Duvall, T.L., Hanasoge, S.M., Jackiewicz, J., Roth, M., Stahn, T., Thompson, M.J., Zharkov, S.: 2009, *Space Sci. Rev.* **144**, 249.
Gopasyuk, O.S., Kosovichev, A.G.: 2011, *Astrophys. J.* **729**, 95.
Haber, D.A., Hindman, B.W., Toomre, J., Bogart, R.S., Larsen, R.M., Hill, F.: 2002, *Astrophys. J.* **570**, 885.
Haber, D.A., Hindman, B.W., Toomre, J., Thompson, M.J.: 2004, *Solar Phys.* **220**, 371.
Hindman, B.W., Haber, D.A., Toomre, J.: 2009, *Astrophys. J.* **698**, 1749.
Howe, R., Komm, R.W., González Hernández, I., Hill, F., Haber, D.A., Hindman, B.W.: 2004, In: Danesy, D. (ed.) *Helio- and Asteroseismology: Towards a Golden Future* **SP-559**, ESA, Noordwijk, 484.
Howe, R., Tripathy, S., González Hernández, I., Komm, R., Hill, F., Bogart, R., Haber, D.: 2011, *J. Phys. Conf. Ser.* **271**, 012015.
Ilonidis, S., Zhao, J., Kosovichev, A.: 2011, *Science* **333**, 993.
Jain, K., Komm, R., González Hernández, I., Tripathy, S., Hill, F.: 2011, In: Choudhary, D.P., Strassmeier, K.G. (eds.) *The Physics of Sun and Star Spots*, *Proceedings IAU Symposium* **273**, 356.
Komm, R.W., Corbard, T., Durney, B.R., González Hernández, I., Hill, F., Howe, R., Toner, C.: 2004a, *Astrophys. J.* **605**, 554.
Komm, R.W., Howe, R., González Hernández, I., Hill, F., Sudol, J., Toner, C.: 2004b, In: Danesy, D. (ed.) *Helio- and Asteroseismology: Towards a Golden Future* **SP-559**, ESA, Noordwijk, 295.
Komm, R.W., Howe, R., Hill, F.: 2009, *Solar Phys.* **258**, 13.
Komm, R.W., Howe, R., Hill, F.: 2011, *Solar Phys.* **268**, 407.
Komm, R., Howe, R., Hill, F., Jain, K.: 2011a, In: Choudhary, D.P., Strassmeier, K.G. (eds.) *The Physics of Sun and Star Spots*, *Proceedings IAU Symposium* **273**, 148.
Komm, R., Ferguson, R., Hill, F., Barnes, G., Leka, K.D.: 2011b, *Solar Phys.* **268**, 389.
Kosovichev, A.G.: 2009, *Space Sci. Rev.* **144**, 175.
Lesieur, M.: 1987, *Turbulence in Fluids*, Kluwer Academic, Dordrecht.
Longcope, D.W., Fisher, G.H., Pevtsov, A.A.: 1998, *Astrophys. J.* **507**, 417.
Mason, D., Komm, R., Hill, F., Howe, R., Haber, D., Hindman, B.: 2006, *Astrophys. J.* **645**, 1543.

Moradi, H., Baldner, C., Birch, A.C., Braun, D.C., Cameron, R.H., Duvall, T.L., Gizon, L., Haber, D., Hanasoge, S.M., Hindman, B.W., Jackiewicz, J., Khomenko, E., Komm, R., Rajaguru, P., Rempel, M., Roth, M., Schlichenmaier, R., Schunker, H., Spruit, H.C., Strassmeier, K.G., Thompson, M.J., Zharkov, S.: 2010, *Solar Phys.* **267**, 1.

Reinard, A.A., Henthorn, J., Komm, R., Hill, F.: 2010, *Astrophys. J. Lett.* **710**, L121.

Schüssler, M., Rempel, M.: 2005, *Astron. Astrophys.* **441**, 337.

Shariff, K., Leonard, A.: 1992, *Annu. Rev. Fluid Mech.* **24**, 235.

van Ballegooijen, A.A., Mackay, D.H.: 2007, *Astrophys. J.* **659**, 1713.

Zhao, J., Kosovichev, A.G.: 2003, *Astrophys. J.* **591**, 446.

Zhao, J., Kosovichev, A.G.: 2004, *Astrophys. J.* **603**, 776.